The 1979 Homestead Valley Earthquake Sequence, California: Control of Aftershocks and Postseismic Deformation

ROSS S. STEIN AND MICHAEL LISOWSKI

U.S. Geological Survey, Menlo Park, California 94025

The coseismic slip and geometry of the March 15, 1979, Homestead Valley, California, earthquake sequence are well constrained by precise horizontal and vertical geodetic observations and by data from a dense local seismic network. These observations indicate 0.52 ± 0.10 m of right-lateral slip and 0.17 ± 0.04 m of reverse slip on a buried vertical 6-km-long and 5-km-deep fault and yield a mean static stress drop of 7.2 ± 1.3 MPa. The largest shock had $M_s = 5.6$. Observations of the ground rupture revealed up to 0.1 m of right-lateral slip on two mapped faults that are subparallel to the modeled seismic slip plane. In the 1.9 years since the earthquakes, geodetic network displacements indicate that an additional 60 ± 10 mm of postseismic creep took place. The rate of postseismic shear strain (0.53 ± 0.13 μrad/yr) measured within a 30×30-km network centered on the principal events was anomalously high compared to its preearthquake value and the postseismic rate in the adjacent network. This transient cannot be explained by postseismic slip on the seismic fault but rather indicates that broadscale release of strain followed the earthquake sequence. We have calculated the postearthquake stress field caused by the modeled coseismic slip. We assume that failure is promoted when the sum of the shear stress plus 0.75 times the fault-opening stress increases. Most aftershocks concentrate at points where the stresses are enhanced by 0.3 MPa (3 bars) or more; aftershocks are nearly absent where postearthquake stresses decrease by 0.3–0.5 MPa. Isolated off-fault clusters of aftershocks that locate at one fault length from the rupture plane are explainable by this hypothesis. We find that ground rupture and postseismic creep take place where near-surface stresses are calculated to increase within the preexisting fault zones. Two patches that extend 4 km from both ends of the seismic fault exhibited neither aftershocks nor measurable postseismic creep. The sensitivity of aftershocks and ground rupture to changes in stress that are less than 5% of the earthquake stress drop demonstrates that the region around the earthquakes was within a few percent of its failure threshold before the main shocks. The preearthquake stress field and the stress required for failure must also have been nearly uniform.

INTRODUCTION

After the Homestead Valley, California, earthquake sequence of March 15, 1979 ($M_L = 4.9, 5.2, 4.5,$ and 4.8), widespread and prolonged aftershock activity spanned a 15×25-km area centered on the 4-km-long surface rupture. The Homestead Valley earthquakes occurred among parallel en echelon faults that display evidence for right-lateral slip during the Quaternary [*Jennings*, 1975]. The faults strike north-northwest, parallel to the average strike of the San Andreas fault in California (Figure 1). Local and large-aperture geodetic observations following the earthquake (Figure 2) reveal a pattern of near-surface fault creep and a broad zone of postseismic shear strain. These observations motivate our study of the focal and regional processes that control aftershocks and postseismic deformation within the upper crust. Because the Homestead Valley earthquakes occur at depths above 5 km, the sequence provides an opportunity to examine with unusual precision postseismic adjustments free of the influence of asthenospheric or lower lithospheric viscous coupling. The seismic and geodetic observations accompanying the earthquake are presented first. We develop a model of the coseismic fault parameters as a guide to the interpretation of the postearthquake stress field, the aftershocks, and the surface deformation. The postseismic observations are then discussed in terms of fault slip, regional strain, and their implications for the preearthquake stress field.

EARTHQUAKE PARAMETERS

Preseismic period. Leveling and trilateration surveyed 1 year before the Homestead Valley earthquake showed no evidence of anomalous deformation. The observations are very limited spatially and do not preclude preseismic displacements as large as 100 mm on a fault plane less than 3×4 km in size at either end of the future seismic rupture. The preseismic elevation changes from 1969 to 1978 on the 35-km-long route MAIN, releveled 1 year before the earthquake sequence, can be compared to the coseismic changes in Figures 3*a* and 3*b*. Preseismic trilateration of the Joshua net from 1977 to 1978 included no stations closer than 15 km from the epicentral region, all located southeast of Homestead Valley. None of the stations in the network show displacements significant at the 95% confidence level. The network shear strain rate within a 60×60-km triangulation network (Figure 4; Homstead plus Eastern Joshua) surveyed in 1939 and 1965 was $\gamma' = 0.25 \pm 0.11$ μrad/yr (10^{-6} rad/yr), with the maximum right-lateral shear oriented N63°W $\pm 19°$, typical of the rate for southern California [*Savage et al.*, 1981] The rate in the 30×30-km subnet centered on the earthquakes was not significant at 95% confidence.

Coseismic period. The four main shocks occurred on a 6-km-long trend between the Homestead Valley and the Johnson Valley faults mapped by *Dibblee* [1967] (Figure 5). The fault plane solutions for the main shocks are well constrained [*Hutton et al.*, 1980] and show nearly uniform orientations of the nodal planes that average N4°W80°W, rotated about 15° clockwise from the strike of the local fault traces. The first 6 hours of seismicity are also shown in Figure 5. Coseismic elevation changes, measured
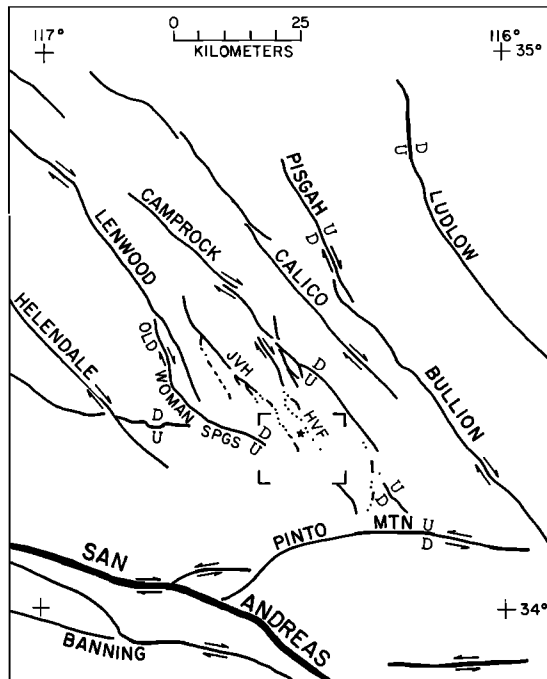
Fig. 1. Setting of the Homestead Valley earthquake showing faults active during the Quaternary [after *Jennings*, 1975]. The corner marks bound Figure 5.

viations represent 5% increases in the model residuals. BM's 27, 32, and 33 on CROSS (Figure 8) had been surveyed in 1957 to second-order (single-run) standards. These marks and BM's 8, 9, 10, 29, 30, and 31 were resurveyed 6 days after the event. Because the 1957 survey of CROSS was not run to first-order standards, the fault-crossing BM's are more poorly measured and less densely spaced than in MAIN. Thus CROSS provides only a weak constraint on the model fault, except to confirm a reverse slip component to the main rupture.

To measure the coseismic shear strain changes, the 1965 triangulation of the five closest stations to the rupture (at distances of 7-18 km) were compared to the 1979+ (postearthquake) trilateration of the same five stations, accomplished 3-5 days after the earthquakes (Figure 4b). We reduced the distances measured after the earthquakes to angles, and these angles were subtracted from the 1965 observations of angles to determine shear strain changes between the two surveys. The total engineering shear strain (γ) and azimuth of maximum right-lateral shear (ψ) can be related to measured strains, using *Prescott*'s [1976] extension of the method of *Frank* [1966]. The strains are referred to a planar coordinate system with the 1 axis oriented east and the 2 axis oriented north:

$$\gamma = [(e_{11} - e_{22})^2 + (2e_{12})^2]^{1/2} \qquad (1)$$

$$\psi = \frac{1}{2} \text{arc tan } [(e_{22} - e_{11})/2e_{12}] \qquad (2)$$

1 year before the earthquake and within 1 month following the event by first-order class I double-run leveling (the standards are specified by the *Federal Geodetic Control Committee* [1980]) along MAIN are presented in Figure 3b. To isolate the displacements presumed to have been caused by the earthquake, the elevations of the end-point bench marks (BM's) are held fixed in Figure 3c. This represents a large and uncertain adjustment to the observed data, amounting to the removal of 0.63-μrad tilt from the line. The elevation changes can be compared to gravity changes for an independent evaluation of this assumption. During each survey, relative gravity with respect to BM D was measured at each site along two closed circuits with sets of three or more gravimeters. Standard deviations are about 10^{-7} m s^{-2} (10 μGal). *Jachens et al.* [1983] found that elevation and gravity changes were correlated for three regions in southern California; a scale factor of -5×10^5 m/m s^{-2} (-5 mm/μGal) provided the best fit. While there is a tendency for positive elevation changes to be associated with negative gravity changes in Figure 6, no consistent scale factor will fit the data. The absence of a correlation in the Homestead area leaves uncertain the proper interpretation of the long baseline tilts in the leveling data; they may reflect unassessed error.

The earthquake displacements were modeled by edge and screw dislocations in an elastic half space, following *Mansinha and Smylie* [1971]. Because the four main shocks appear coplanar and share a similar nodal plane orientation, we treated the main shocks as producing slip on one fault surface. We chose a rectangular model fault that passes through the four main shock hypocenters. This leaves the slip vector and the upper and lower edge of the fault plane to be modeled. Trial-and-error modeling to fit the coseismic leveling data from MAIN and CROSS resulted in a net slip u of 0.57 ± 0.08 m, with a right-lateral to reverse slip ratio of 3, on a buried fault that extends from 0.75 ± 0.25 km below the ground to a depth of 5 km (Figure 7). The de-

From (1) we resolve the shear strain rate, $\gamma' = \gamma/\text{yr}$; γ' and ψ are plotted in Figure 4.

Large uncertainties in the measured angles, combined with the limited number of angle observations within the Homestead subnet, leave the network shear strains poorly determined. The 10 angle observations were used to obtain a least squares estimate of the right-lateral slip on the same fault model used with the leveling data. This inversion of the angle changes results in a right-lateral slip of 0.46 ± 0.27 m. Three measurements of line length made 1 year before the main shocks sequence and 3-5 days following them provide a further constraint on the fault slip. Because the lines locate 12-40 km southeast of the main shocks, they are not very sensitive to the fault parameters. If models are restricted to the 6 × 4.25 km ($L \times W$) fault plane of Figure 7, $u = 0.55 \pm 0.35$ m.

The three estimates of the coseismic fault slip from leveling, triangulation, and trilateration cover different periods but give approximately the same result. The weighted average net slip from these observations is 0.56 ± 0.11 m. The coseismic fault parameters are summarized in Table 1. The seismic moment M_0 calculated from the average fault model listed in Table 1 is (4.2 ± 0.8) × 10^{17} N m (× 10^{24} dyne cm). The seismic moment can also be obtained from conversion of M_L and M_s for the four main shocks by the empirical relations of *Thatcher and Hanks* [1973] and *Hanks and Kanamori* [1979], which yields 3.6 × 10^{17} N m, indistinguishable from the geodetic moment. The good agreement between the independent geodetic and seismic estimates of M_0 argues that the product of $u \times A$ (mean fault slip times fault area) calculated for the coseismic model is approximately correct. Since the fault length is delineated by the four coplanar main shocks and the leveling data, and the fault depth is approximately constrained by the deepest aftershocks to be 5 km, the agreement between geodetic and seismic moments means that our estimate of u should be accurate to about 25%.
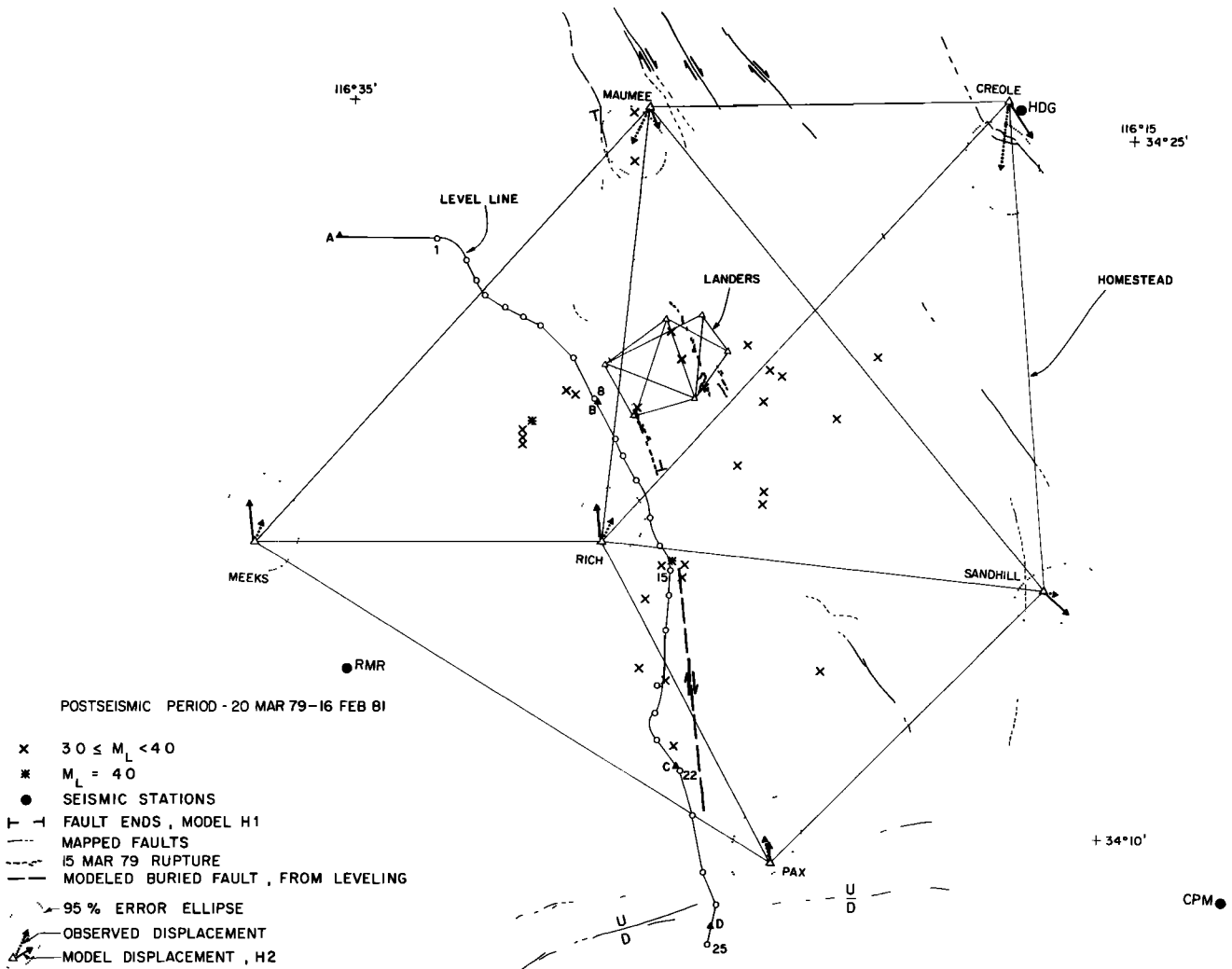
Fig. 2. Landers (inset) and Homestead networks, with inner coordinate solution for Homestead displacements.

For a roughly circular fault area, the mean static stress drop $\Delta\sigma_s$ of the earthquake sequence is proportional to u/A, the ratio of mean slip to fault area. Following *Kanamori and Anderson* [1975], the static stress drop for this earthquake is 8.5 ± 1.2 MPa (85 bars); correction for the effect of the free surface according to *Boore and Dunbar* [1977] reduces $\Delta\sigma$ to 7.2 ± 1.0 MPa, somewhat larger than is usual for upper crustal earthquakes.

POSTSEISMIC PERIOD

Seismicity. Aftershocks concentrated along the trend formed by the four main shocks and also within isolated clusters off the main shock trend (Figures 9a and b). Aftershocks are abundant at very shallow depths. This pattern developed within 1 day of the first earthquake in the Homestead sequence with no outward migration of aftershocks with time [*Hutton et al.*, 1980]. There is a remarkable paucity of aftershocks on those segments of the Johnson Valley and Homestead Valley faults upon which ground rupture took place. D. Given (written communication, 1981) relocated 300 aftershocks recorded by the dense local array shown in Figure 5 with respect to a master event; the epicenters showed no significant location changes. Fault plane solutions for five events in the eastern and western aftershock clusters are all con-

sistent with a least principal stress oriented north-northwest. This axis is also appropriate for the four main shocks. Two solutions show right-lateral slip on vertical planes, and three show a component of normal slip.

Near-fault geodetic observations. Within 4 days after the earthquake, the Landers trilateration net was emplaced to observe postseismic horizontal surface displacements in a 3 × 5-km area centered on the main shock epicenters, extending over the surface ruptures (Figure 10). Observations of line length were performed following the procedure explained by *Lisowski and Prescott* [1981]. Resurveys were carried out 4 days, 0.9 year, and 1.9 years after the earthquakes. To assess the internal consistency of the line length observations relative to their errors, we calculated the rms signal strength, (S). The derivation of (S) is presented in the appendix. Briefly, (S) is the ratio of the rms weighted observations to a least squares measure of observation and network configuration errors. For the 1.9-year postseismic period, (S) = 4.5σ; the observations are over 4 times larger than the uncertainties. (S) is significant at the 96% confidence level. The inner coordinate solution [*Brunner*, 1979] for the station displacements is shown in Figure 10. Because we lack a reference frame external to the network, we require the center of mass of the stations to be stationary and prescribe no net rotation about this center.
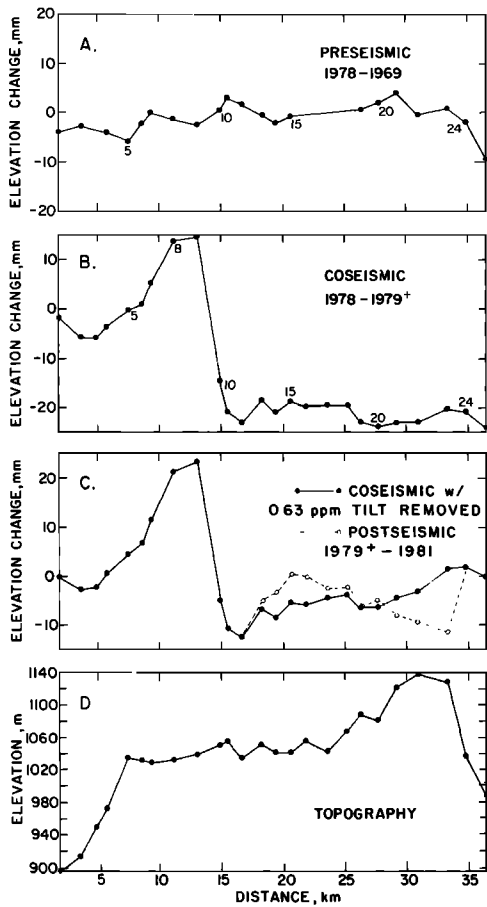
Fig. 3. Sequence of elevation changes along MAIN. (a) Preseismic changes, (b) Observed coseismic changes, (c) Coseismic changes with end-point elevations fixed (solid line) and with postseismic 1979-1981 changes shown (dashed line), (d) Route topography.

These assumptions are needed only to represent station displacement vectors; the model fitting to be discussed employs the line length changes rather than calculated station displacements.

The principal strain changes for the postseismic period reveal large values of shear strain and negative dilatation, dominated by north-south contraction (Figure 11; Landers is the small inset network). However, these results are subject to large standard deviations. The deviations are partially caused by fault slip at the surface, which produces a nonuniform strain field. Errors in areal dilatation ($\Delta = e_{11} + e_{22}$) can be large because an error in the length standard of the initial or final survey contributes an apparent dilatation, but such a fixed error would have a smaller effect on the determination of shear strain [Savage and Prescott, 1973]. Also (S) does not necessarily measure the fixed error. Because some networks smaller than Landers that are not in earthquake focal regions show excursions in dilatation comparable to Landers [Prescott et al., 1981; Savage et al., 1981], the significance of the Landers postseismic compression is difficult to judge.

Elevation changes were measured along MAIN 20 days and 600 days after the main shocks (Figure 3c).The 6-km-long route, CROSS, was resurveyed 6 and 56 days after the main shocks; the profile of elevation change is shown in Figure 8. Here, the elevation of BM 10 is held fixed because it is farthest from the main shock. Five to ten millimeters of relative subsidence can be seen above the modeled main fault in contrast to the coseismic displacements. The postseismic tilt between BM's 8 and 10 (Figure

7) reversed from the period 27-62 days to 62-585 days after the main shock, but the change in tilt is not significant at the 95% confidence level.

Large-scale deformation. Following the earthquakes, the Joshua trilateration net was extended across Homestead Valley by inclusion of the 1939/1965 triangulation stations. This six-station subset of the Joshua net, which will be referred to as the Homestead net (Figure 2), was resurveyed along with the Landers net 3-5 days, 0.9 years, and 1.9 years after the earthquakes. The Homestead net circumscribes most of the aftershock zone (Figure 2). Both the Joshua net and its Homestead subset show observations substantially larger than network uncertainties; the rms signal strength (S) for Homestead is 3.7σ; (S) is significant at the 94% confidence level. The total shear strain rate for the full 1.9-year postseismic period reached $\gamma' = 0.53 \pm 0.13$ ppm/yr. The shear is well determined, acts parallel to the fault trends within the network, and is significantly greater than the shear strain rate within the adjacent Joshua network, where no line length is significant at 95% confidence (Figure 11). The principal strains are compressional, with north-south contraction dominant as in the Landers net; the Homestead dilation is $\Delta' = -0.33 \pm 0.21$

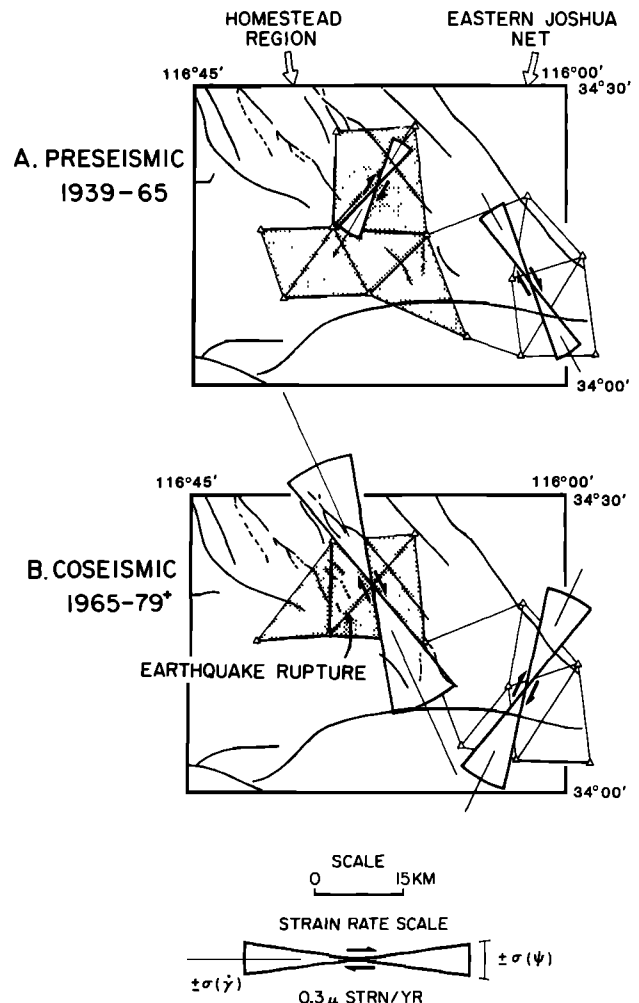## RIGHT LATERAL SHEAR STRAIN RATES

Fig. 4. Right-lateral shear strain rates; γ' is the maximum right-lateral shear strain rate, and ψ is the azimuth of maximum shear strain; 1σ variations in (γ', ψ) are indicated.
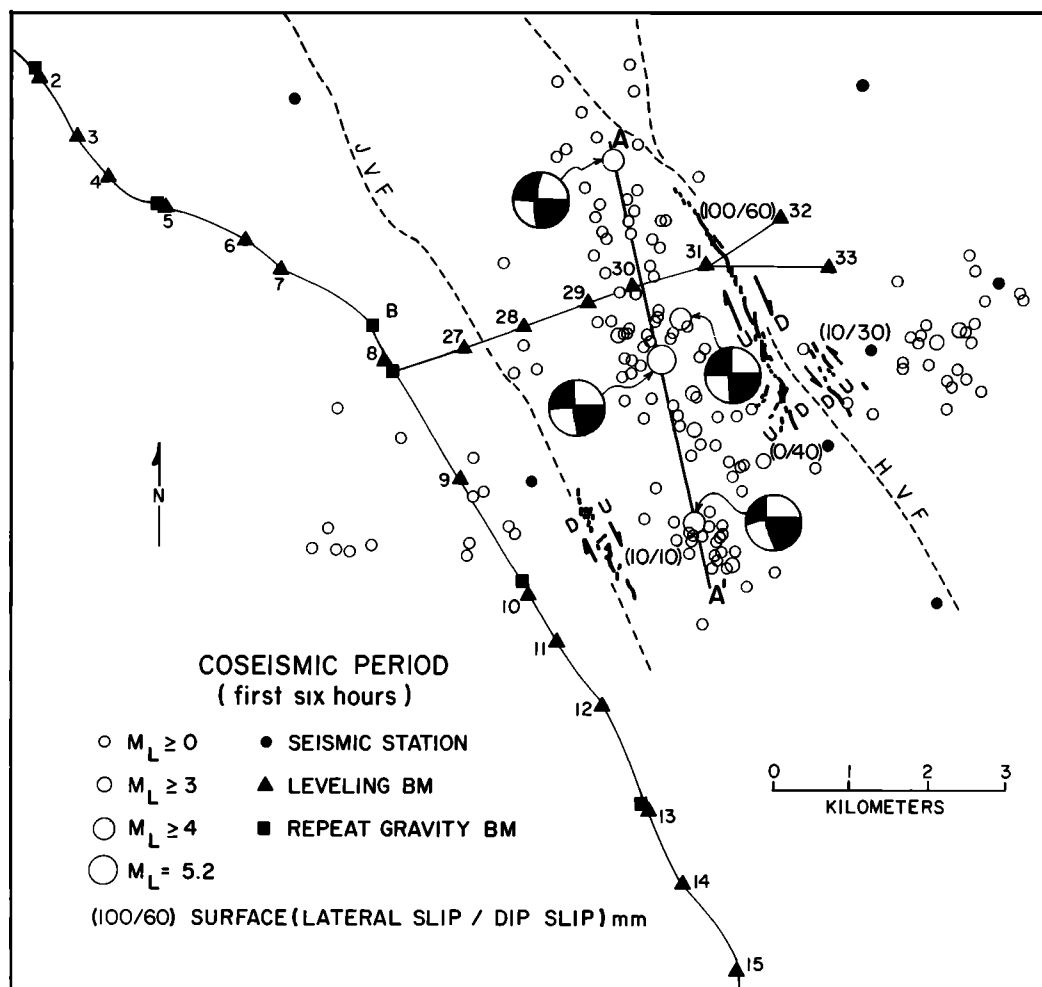
Fig. 5. First 6 hours of aftershocks and fault plane solutions for the main shocks recorded by a portable network described by *Hutton et al.* [1980], with level lines MAIN and CROSS (thin), surface rupture (heavy), and mapped faults (dashed). HVF, Homestead Valley fault; JVF, Joshua Valley fault. The surface trace of the model fault is delineated by A-A'.

ppm/yr. The rate of negative dilatation is roughly constant, lacking the rapid initial decay that was measured within Landers.

Observed changes in elevation along MAIN are shown with route topography in Figure 12. A check for linear elevation- or slope-dependent errors following *Stein* [1981] revealed none. In addition, no rods were changed along this route during either survey, so a linear error could not be masked by changes in field procedure. The elevation of the end points of the leveling line are held fixed in Figure 12b to isolate local elevation changes from the 1-μrad regional tilt along the route. No significant residual postseismic elevation changes were observed nearby or northwest of the epicentral region. However, significant postseismic tilts took place to the south of the main shock where aftershocks are also abundant, between BM's 12 and 25.

DISCUSSION

We pursue two approaches to analyze the aftershocks and postseismic deformation following the Homestead Valley earthquake sequence. First, we use the coseismic fault model to predict the postearthquake stress field and find that aftershocks concentrate where the calculated stresses increase by only a few tenths of a megapascal, while aftershocks are nearly absent where the incremental stresses caused by the main shocks decrease by the same

amount. Second, we model the postseismic trilateration and leveling observations to identify sites of postseismic fault slip. From this we find that the faults which displayed earthquake ground rupture underwent continued near-surface creep and also that widespread shear strain developed over a broad area within the Homestead network. We argue that the broadscale shear could not have resulted from continued slip on the seismic fault plane.

Postearthquake stresses. To test whether the distinct pattern of aftershocks was caused by the stresses imposed by the earthquake fault slip, we calculate the Coulomb fracture criterion and map the postearthquake stress changes around the rupture zone. We seek the shear and normal stress acting on vertical planes that are oriented parallel to the strike of the modeled coseismic slip plane. The condition of plane stress requires that

$$\sigma_{ij} = G [2/3(e_1+e_2)\delta_{ij} + 2e_{ij}] \qquad (3)$$

where (e_1, e_2) are the horizontal principal strains from the coseismic dislocation model, G is the shear modulus, and Poisson's ratio is 1/4. For normal stresses less than 200 MPa, *Byerlee* [1978] found that almost all rocks fail when $\tau_s = -0.85\sigma_n$. Here, τ_s is the shear stress parallel to the fault, and σ_n is the out-
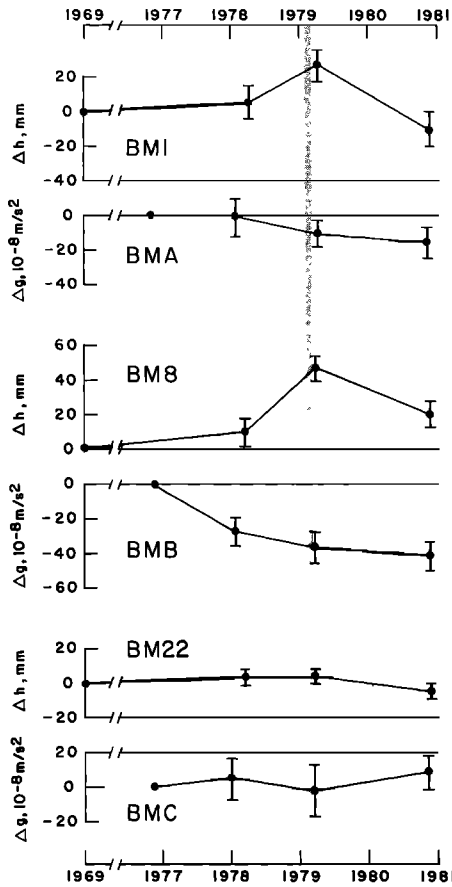
Fig. 6. Comparison of gravity and MAIN elevation changes without removal of trends in the leveling data. Elevation and gravity changes are with respect to BM's 24 and D in Figure 2, respectively (10^{-8} m s^{-2} = 1 μGal).

ward normal or fault opening stress. Incipient failure or the initiation of inelastic behavior takes place when $\tau_s \sim -0.6\sigma_n$. Because it is uncertain which condition applies to the aftershocks and postseismic creep, we use a Coulomb criteria of $\tau_s = -0.75\sigma_n$. Thus we assume that failure is promoted by the same amount when τ_s increases by 0.75 MPa or when σ_n increases by 1 MPa. Values of $(\tau_s + 0.75\sigma_n)$ are calculated from (3) under the assumption that $G = 3 \times 10^{-6}$ MPa.

We calculated the Coulomb stresses at the ground surface acting on vertical planes only. More complex calculations for inclined planes at depth did not seem warranted because the aftershock pattern is nearly uniform with depth (Figure 9b) and because the coseismic model fault is nearly vertical. We also neglect the small reverse component of coseismic slip because we consider only the horizontal component of shear stress in the Coulomb fracture criterion. In other words, we treat the main shocks and aftershocks as pure right-lateral slip events on vertical faults striking N5°W. While this is an oversimplifcation, we note that some of the aftershocks form N5°W striking trends, such as those in the off-fault cluster west of the model fault.

The pattern of postearthquake stress changes shown in Figure 9a can best be thought of as the addition of two stress fields. The shear stress change parallel to the main fault, τ_s, produces the large elongate stress peaks beyond the fault ends and the two smaller peaks off the main fault. The correlation between the predicted off-fault shear stress maxima and aftershocks has been pointed out by Hamilton [1972], Brown et al. [1973], and Das and Scholz [1981], who recognized the correlation for the Homestead Valley earthquakes. Chinnery [1963] calculated the shear stress distribution with depth for a rectangular strike slip dislocation and found that the off-fault stresses diminish with depth, while the shear stress at the fault ends increases in magnitude at the base of the fault. The stress acting normal to the fault plane or the fault-opening stresses, σ_n, exhibit a roughly quadrantal distribution except just beyond the fault ends, where the normal
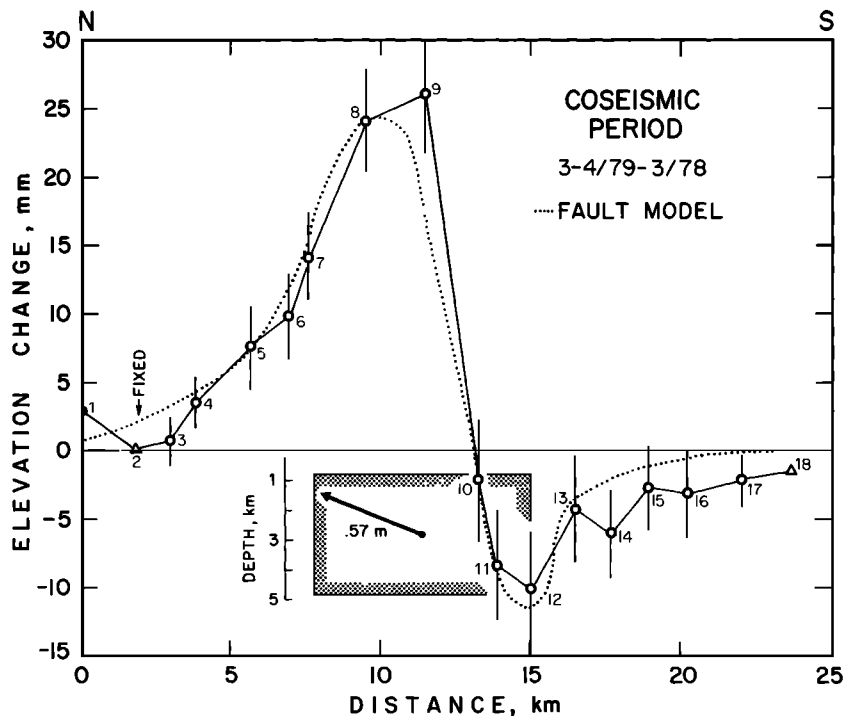

Fig. 7. Elevation changes along MAIN, with uniform tilt removed. The dislocation fault model is shown with elevation changes predicted for the model. The distance along the leveling line is shown, which exaggerates the fault length.

TABLE 1. Coseismic Dislocation Model

Source of Data	Measurement Period	Strike/Dip	Net Slip, m	Right/Reverse Slip	Upper Depth, km	Lower Depth, km	Length, km	M_0, N m	$\Delta\sigma_s$, MPa
Main Shocks	March 15, 1979	N4°W80°S[a]	ND	8[a]	ND	5.0[b]	6.0[c]	3.6×10^{17}	ND
Releveling	1978.3–1979.3	N10°W85°S	0.57+0.08	2	0.75+0.25	+	+	4.2×10^{17}	7.2+0.7
Triangulation	1965.0–1979.3	N6°W90°d	0.46+0.27	(right only)	+	+	+	ND	ND
Trilateration	1978.1–1979.3	N6°W90°d	0.55+0.35	(right only)	+	+	+	ND	ND
Model		N6°W85°S	0.56+0.11	3+1	0.75+0.25	5.0	6.0	$(4.2+0.8)\times10^{17}$	7.2+1.3

ND, no data; pluses indicate assumed as above.

a Mean of four main shocks
b From hypocenters
c From epicenters
d Assumed

FAULT CROSSING RELEVELS

COSEISMIC MODEL

no coseismic tie

1972 tie

COSEISMIC PERIOD includes first 6 days after mainshock

ELEVATION CHANGE, mm

POSTSEISMIC 6-56 days after shock

10mm horiz / 10mm vert

100mm horiz / 40mm vert

.52 m horiz / .17 m vert

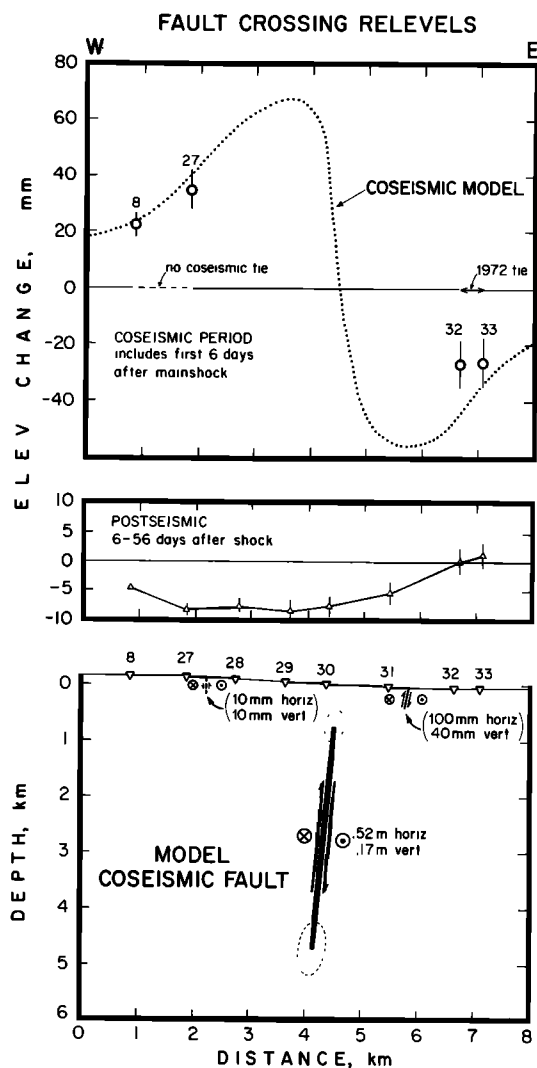MODEL COSEISMIC FAULT

DEPTH, km

DISTANCE, km

Fig. 8. Fault-crossing elevation changes along CROSS for the coseismic period (top), postseismic period (middle), and source model (bottom). The earthquake surface offsets are shown between BM's 27 and 28 and between 31 and 32.

stresses depart from the simple pattern and reverse sign. When the τ_s and σ_n fields are added, the off-fault peaks migrate into the dilatational quadrants, and the fault end peaks rotate slightly into the compressive quadrants. Kadinsky-Cade and Willemann [1982] have also suggested this explanation for the spatial pattern of off-fault aftershocks.

We find the correlation between the Coulomb stresses and the aftershocks to be persuasive evidence that the earthquake-induced stress changes control aftershocks. Four features of the correlation strike us as important. First, aftershocks concentrate where the predicted stresses increase more than 0.3 MPa, or less than 5% of the static stress drop, $\Delta\sigma_s$. Second, aftershocks are nearly absent where stresses decrease by more than a few tenths of a megapascal, with the exception of the southeastern quadrant, where the predicted stresses drop by 0.5-0.8 MPa in the presence of aftershocks. Third, aftershocks are conspicuously absent in the regions of high stress immediately beyond the fault ends for an interval of about 4 km. These regions sustained predicted stress increases of up to about 2.5 MPa without producing aftershocks. The coseismic elevation changes preclude significant displacements in these regions. Modeling of the observed strain changes
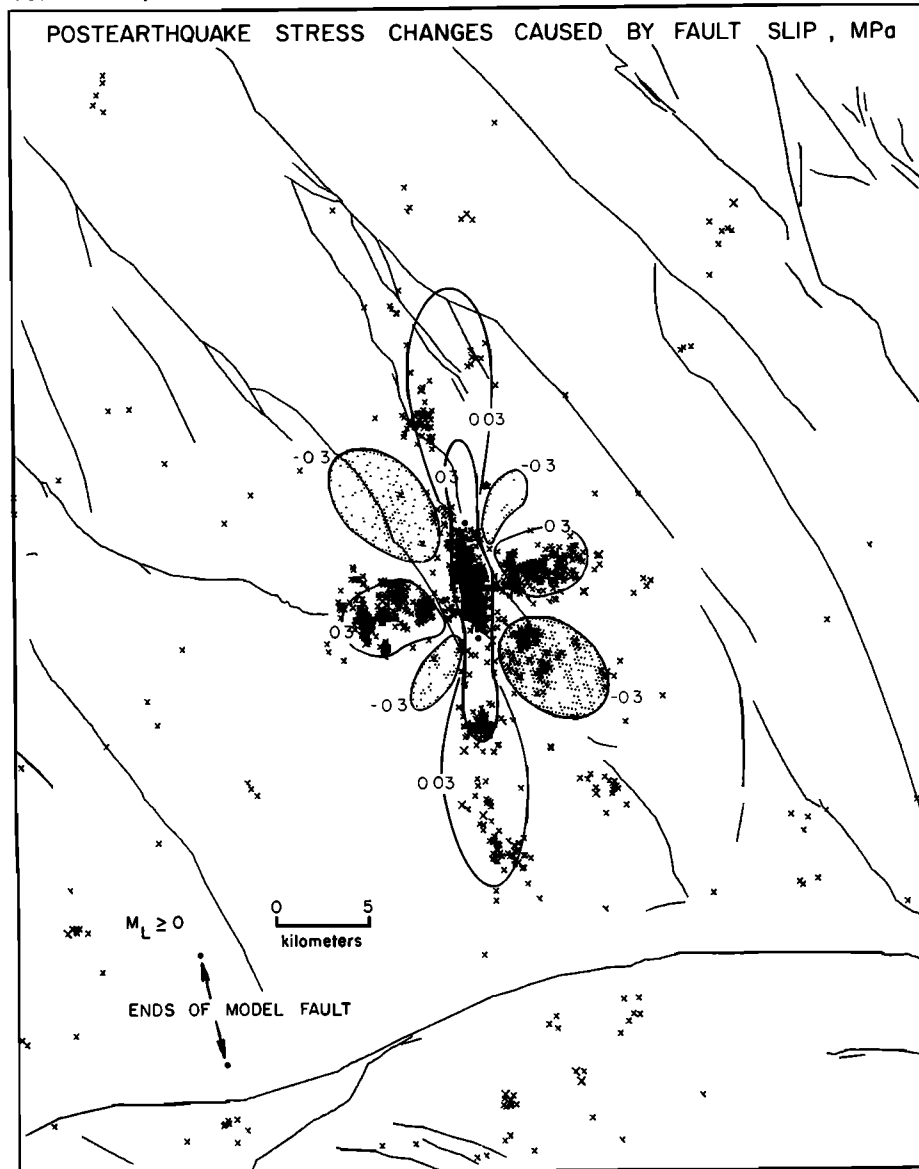
HOMSTEAD, 3/20/79 TO 2/10/81

Fig. 9a. California Institute of Technology epicenters for $M_L > 0$, March 20, 1979, to February 10, 1981, with Quaternary faults. Calculated failure stress increases (solid perimeter) and decreases (stippled areas) are contoured.

will show that no detectable aseismic slip took place within these zones during or following the earthquake sequence. Fourth, aftershocks farthest from the main shock epicenters (greater than one fault length from the fault ends) locate where the stresses are predicted to increase 0.05-0.1 MPa, or about 1% of $\Delta\sigma_s$, although our free surface calculation probably underestimates the stresses at the depth beyond the fault ends.

The segments of the Homestead Valley and Johnson Valley faults that ruptured during or following the principal sequence lie within areas of increased near-surface stress. In contrast, neither fault produced measurable offsets at the surface in regions of predicted surface stress decrease. The 1.5-km segment of the Johnson Valley fault that showed about 10 mm of coseismic surface offset [Hill et al., 1980] is located where the predicted stress increased about 0.2 MPa (2 bars). The 50- to 100-mm ground displacement measured on the Homestead Valley fault [Hill et al., 1980] occurred where we predict the stress to increase about.

0.3-1.2 MPa. The spatial correlation between fault slip and the predicted stress acting on the fault suggests to us that ground rupture takes place where high stresses cause favorably oriented zones of weakness near the surface to displace. Thus the surface rupture zones need not connect to the main coseismic fault at depth, and the slip measured at the surface (10-100 mm, predominantly right lateral) need not represent the slip at depth (which we model as about 0.55 m). The modeling to follow will show that postseismic slip on the Homestead Valley and Johnson Valley faults did not extend to depths of 2 km. The Homestead Valley and Johnson Valley fault slip appears to be nearly aseismic; few aftershocks locate on either zone of ground rupture. Perhaps the fault zone is too weak to accumulate significant stress, as Scholz et al. [1969] suggested to explain near-surface creep following the Parkfield earthquake, and instead slips where it passes through regions of high strain. The rock adjacent to the faults may be strong enough to maintain high stresses at depths of a
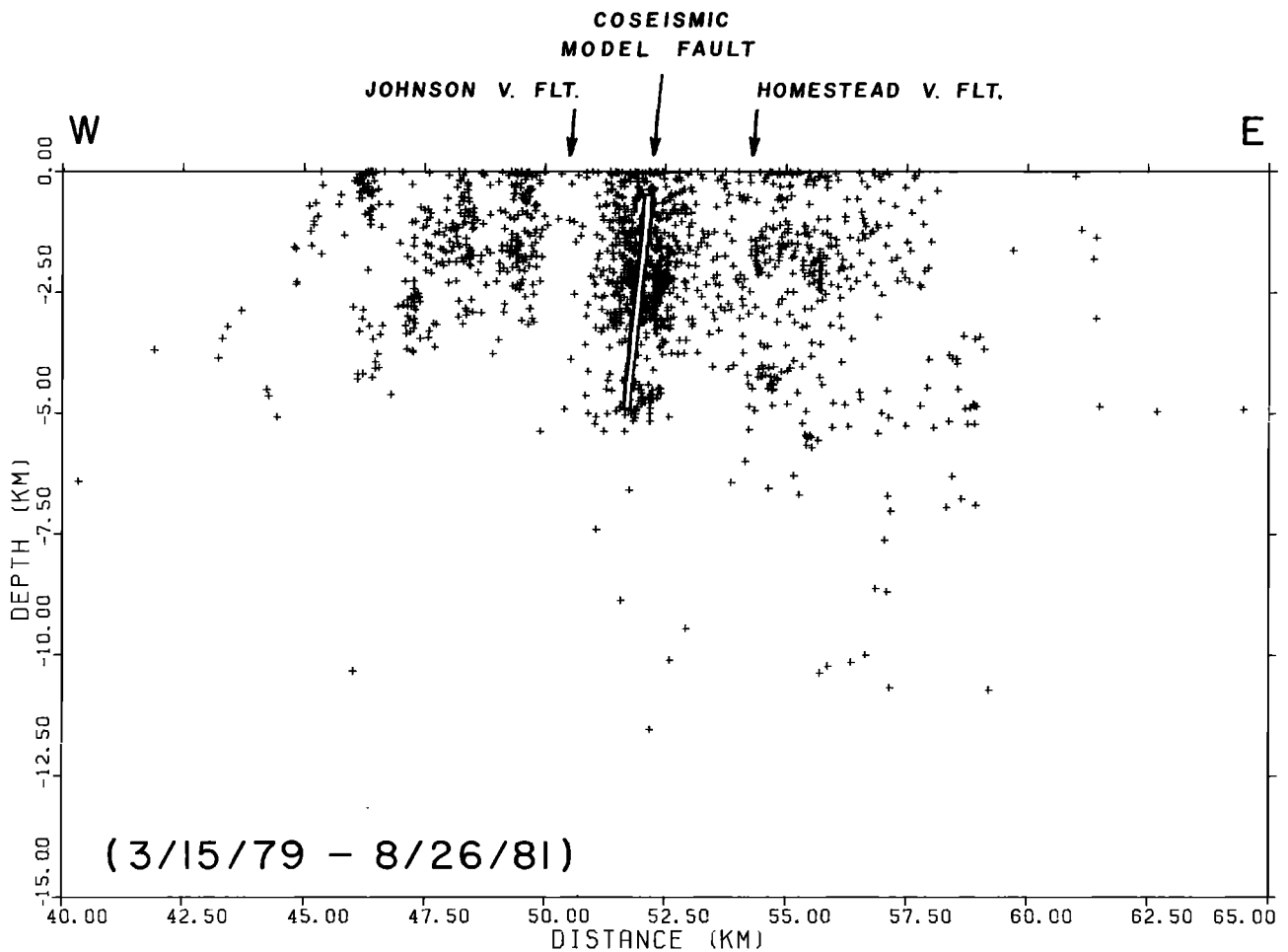
Fig. 9b. An east-west cross section of quality A hypocenters for $M_L > 0$ from March 15, 1979, to August 26, 1981.

kilometer or more, giving rise to stick slip behavior and aftershocks.

We reach the general conclusion that the good correlation between postearthquake stress changes, aftershocks, and ground rupture means that the preearthquake stress level must have been nearly uniform and close to the failure threshold over a broad area. It is, however, remarkable that beyond the north end of the fault, neither surface nor seismic rupture took place. Here the Homestead Valley fault is colinear with the trend formed by the main shocks; predicted Coulomb stresses increase up to 1.2 MPa. We experimented with coseismic models in which the slip tapered at the ends, but this did not remove the zones of elevated stress beyond the fault ends. The absence of aftershocks and ground rupture may be explained by a preearthquake stress level about 1 MPa lower than the surrounding region or by rocks that are stronger than those elsewhere in the region. What we can state is that the regions beyond the fault ends produced neither earthquakes nor fault slip during or following the main shock sequence. The preearthquake stress could have been reduced by 1 MPa if the 4- to 5-km-long segments beyond the fault ends had sustained displacements in the past, although no earthquake of $M_L \geq 5.5$ took place within 35 km of the main shock epicenters during the 123-year period 1857-1979 [Moths and Ellsworth, 1980].

Near-fault modeling. Ruptured ground was observed on the first day of the earthquake sequence by *Hill et al.* [1980] along

three segments of two parallel faults. These zones proved to be sites of postseismic creep. We modeled the length change observations (11 lines) of the Landers network for the fault parameters, and the goodness of fit was judged by the percent of the signal explained by the model (M) and its probability distribution. The derivations are given in the appendix. The zones of ground breakage along the Homestead Valley and Johnson Valley faults [Hill et al., 1980] were used to fix the fault locations and length. The same fault parameters were applied to all three faults. The upper depth of the faults was fixed at 175 m. Four parameters, the net fault slip, slip angle (right/reverse slip), dip, and the lower fault depth were varied in numerous trials to obtain a best fit model, L1. L1 explains 63% of the observations. The faults and the station displacements are shown in Figure 10, and the fault parameters are listed in Table 2. The deviations in the fault parameters in Table 2 reflect five percent departures in the model fit (M). The unexplained 37% of the signal may be related to the large but poorly constrained network compression ($\Delta = -4.4 \pm 2.3$ ppm) that cannot be modeled by strike slip faulting. Model L1 imposes a significant component of reverse slip on the postseismic faults (right/reverse slip = 2). Although this result is consistent with the fault plane solutions for the earthquake sequence and the record of surface displacements on the Homestead Valley fault, it is not supported by the postseismic releveling across the fault zone that shows no evidence for reverse slip during the first 60 days.
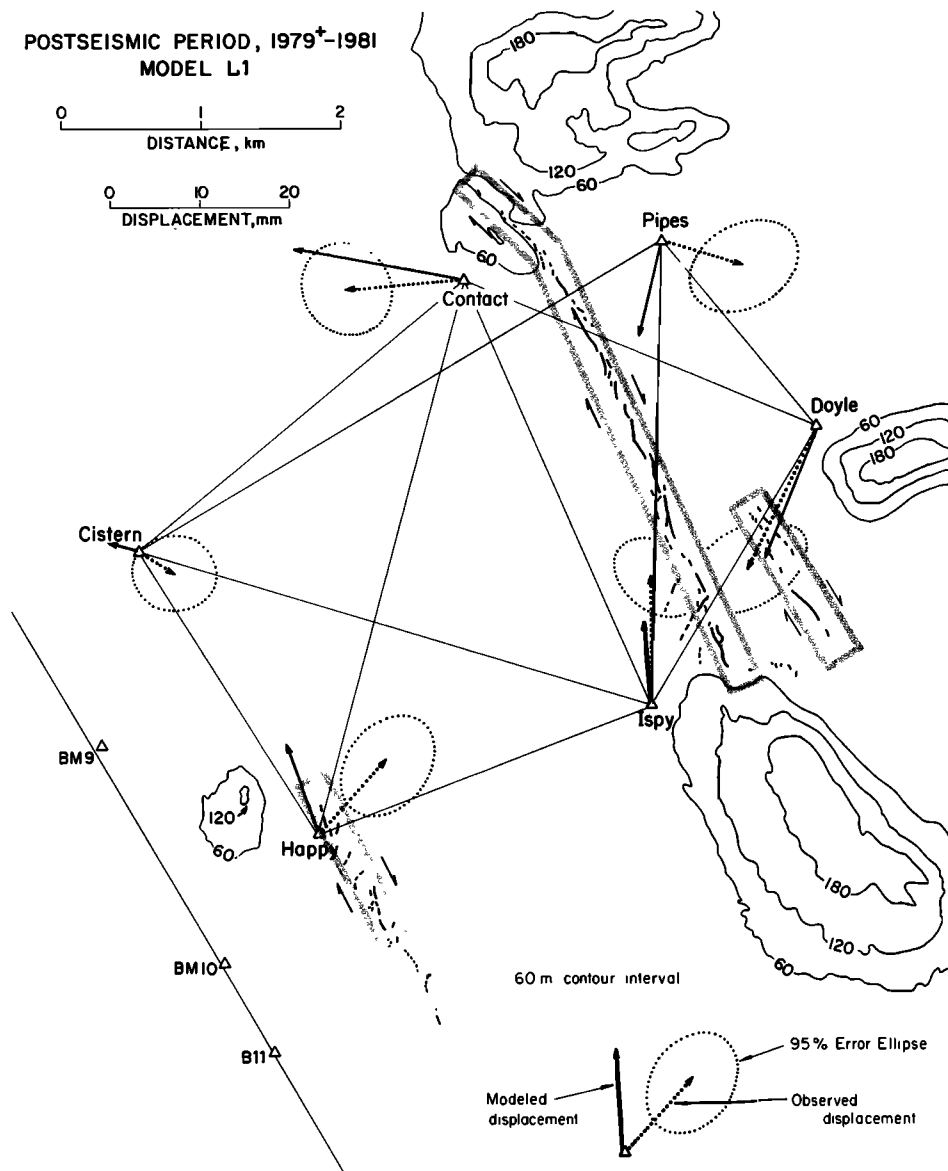
Fig. 10.   Landers trilateration network, showing an inner coordinate solution for 1979-1981 station displacements, and faults for model L1.

Because about 75% of the aftershocks locate on the coseismic fault plane, we tested whether the seismic fault sustained appreciable postseismic slip. We found that adding 20 mm of right-lateral and reverse slip to L1 reduced the overall fit (M) by 5%; (M) deteriorated substantially if slip on the seismic plane increases beyond this amount. The cumulative moment of the aftershocks that locate on the coseismic fault plane during the 1.9-year postseismic period is approximately 4×10^{15} N m, by conversion from M_L. If this moment is imposed on the coseismic fault, it would be equivalent to a slip of 10 mm $(u = M_o/\mu LW)$; about 10 mm of postseismic slip on the seismic fault plane is therefore consistent with the aftershocks and the trilateration.

The key feature of the postseismic deformation measured by the Landers network are near-surface slip along the ruptured segments of the mapped fault zones, with a magnitude of about 10% of the coseismic displacement. This process was almost fully aseismic, occurring in the fault zones above a 2-km depth. The 5-km-deep coseismic fault plane slipped no more than a few tens

of millimeters after the earthquakes. Any slip on this fault was probably released by aftershocks.

Large-scale modeling. The rms signal strength (S) of the Homestead network postseismic observations is 3.7σ. We first used the three near-surface faults of the Landers model L1 to see if these alone would adequately explain the Homestead network length changes. The (M) for this model, HØ, is only 12%, indicating that the near-surface faults are insufficient to model the Homestead observations. There is a 92% probability that this model fits the observations no better than chance. The large and well-determined postseismic shear strain changes (Figure 11) oriented parallel to the regional fault strike suggest either a crustal fault much longer than the coseismic fault plane, or uniform shear over the entire network. Model H1 is our best fit solution for a single fault at seismic depths. We constrained the fault to have a vertical dip and right-lateral slip. We solved for the slip (60 ± 10 mm), upper and lower depth (0.6-6.0 km), and length (13 km). The optimal model fault did not extend into the southern

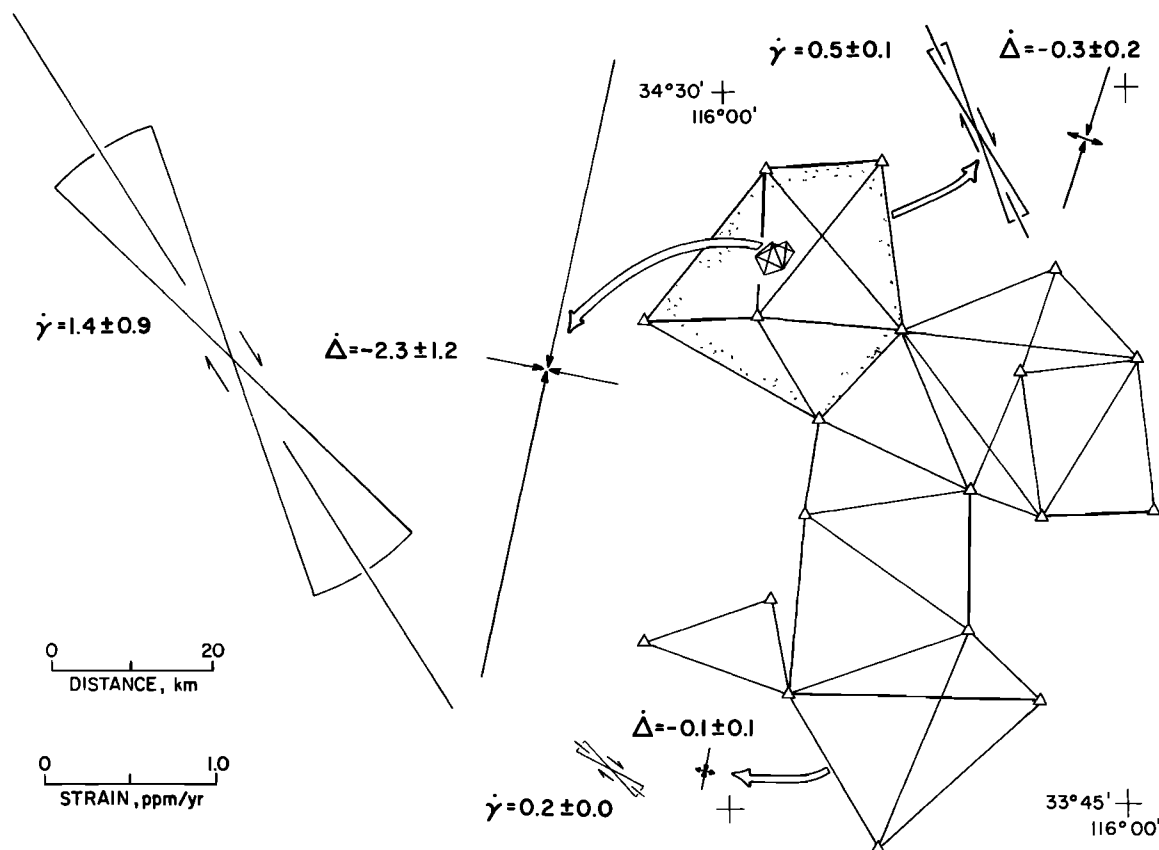## POSTSEISMIC PERIOD STRAIN RATES, ppm/yr, 1979*-81

Fig. 11. Network principal and right-lateral shear strain rates for Landers (inset network), Homestead (dotted), and Joshua (all else).

half of the network (see Figure 2 for the fault location). However, the model explains only 43% of the signal (*M*). Model H2 distributes shear strain across the Homestead network. We model the shear by imposing 60 mm of slip on a fault buried from 7 to 100 km in depth. We do not claim that such a fault exists; rather the deep fault model is a convenient vehicle to produce shear that is only slightly peaked in the center of the network. The (*M*) for model H2 is also 43%. Thus neither a crustal fault nor distributed shear adequately explains the Homestead observations.

The leveling route MAIN passes nearby the southern aftershock zone between BM's 15 and 22. The detrended leveling observations (Figure 12b) show elevation changes consistent with 50-100 mm of buried strike slip on a crustal fault. To fit the leveling data, the fault ends are placed beside the maximum positive and negative elevation changes. This leaves a 4-km-long unslipped patch between the coseismic fault segment and the postseismic slip zone.

Combined model. We use the observations of both the Landers and Homestead networks to compare the fit of the crustal fault and distributed shear models when combined with the near-surface fault slip of model L1. Because the Landers and Homestead networks share no common stations, the rms signal strength is small; (*S*) = 2.2σ. The fit for model LH1 (L1 + H1) is 44%. The crustal slip beyond the coseismic fault ends causes the Landers residuals to increase. Model LH2 (L1 + H2) produces a fit of 83%; while the fit is better than for either L1 or H2 alone, the formal probability gain of LH2 over LH1 is 10% (Table 2). The

success of LH2 is caused by the broad shear zone, which improves both the Landers and Homestead residuals, and the absence of significant slip on the seismic fault plane at depths below 2 km.

The required features of a model that properly reproduces the 1.9-year postseismic observations on both the Landers and Homestead scales are (1) near-surface creep of about 10% of the seismic slip within the Homestead Valley and Johnson Valley fault zones, (2) no seismic or aseismic slip greater than 20 mm on the seismic fault plane or the segments beyond the fault ends for 4 km, and (3) distributed shear of about 1 μrad over an area at least as large as the Homestead network.

CONCLUSIONS

The Homestead Valley earthquakes took place within unusually dense geodetic and seismic networks. Following the earthquake sequence, the focal region was intensively monitored for surface deformation and aftershocks. The seismic and postseismic displacements are well constrained by leveling, triangulation, trilateration, and geological observations. The salient features of the event are the swarmlike character of the four nearly coplanar shocks of $M_L = 4.5 - 5.2$, the high mean static stress drop ($\Delta\sigma_s = 7.2 \pm 1.3$ MPa) and the high shear strain rate during the 1.9-year period after the main shocks. The postseismic rate of shear strain within the 30 × 30-km Homestead network centered on the rupture is 0.53 ± 0.13 μrad/yr. This is significantly greater than

TABLE 2. Summary of Postseismic Trilateration Models

Model	Network	Network rms Signal Strength (S)	Confidence Level of Signal (S₁), %	Dislocations Modeled	Percent of Signal Explained by Model (M), %	Confidence That Model Can Be Rejected (M₁), %
L1	Landers	4.5σ	96	3 near-surface faults	63	82
H0	Homestead	3.7σ	94	3 near-surface faults	12	92
H1	Homestead	3.7σ	94	1 crustal fault	43	85
H2	Homestead	3.7σ	94	distributed shear	43	85
LH1	Landers and Homestead	2.2σ	68	3 near-surface faults and 1 crustal fault	44	55
LH2	Landers and Homestead	2.2σ	68	3 near-surface faults and distributed shear	83	45

Dislocations	Slip, m	Right/Reverse Slip	Dip, deg	Upper Depth, km	Lower Depth, km	Length, km
3 surface faults	0.06±0.01	2±0.8 (right only)	70±15	0.175	1.5±0.8	1.4, 1.8, 4.2
1 crustal fault	0.06±0.01	(right only)	90	0.6±0.2	6.0±2.5	13.0
Distributed shear	0.06±0.01		90	7.0	100.	100.

the 1939-1965 preseismic shear strain rate in the same network (0.10 ± 0.08 μrad/yr), and the 1.9-year postseismic rate in the adjacent Joshua network (0.20 ± 0.04 μrad/yr). We find it very unlikely that the postseismic transient was caused by slip on the seismic fault or its northern or southern extensions. It seems equally remote that a 5-km-deep earthquake could produce measurable viscoelastic rebound. Pure shear over the network area, or a few millimeters of right-lateral slip along each of the faults in the network, however, could produce such a strain increment.

Calculation of the postearthquake stresses acting on planes parallel to the main rupture reveals four fundamental features of the earthquake process:

Off-fault aftershock clusters. Aftershocks concentrate where stresses are locally raised by 0.3 MPa (3 bars), or just 4% of $\Delta\sigma s$; aftershocks are generally absent where the postearthquake stresses decrease by 0.3 MPa or more. The isolated off-fault aftershock clusters provide a strong test of this hypothesis because they are located away from the fault surface or fault tips, regions which may be subject to high stress intensities. We predict that when $\Delta\sigma_s$ exceeds about 5 MPa, vertical strike slip earthquakes with equidimensional fault planes should display the off-fault clusters. The extent to which the clusters locate in the dilatant strain quadrants demonstrates the role of both the shear stress and the normal stress changes in the failure of rocks.

Preearthquake stress level. We interpert the association of aftershocks with stress increases of just 0.3 MPa to mean that the the region was very close to its failure stress before the earthquake. In addition, the good correlation between calculated stress
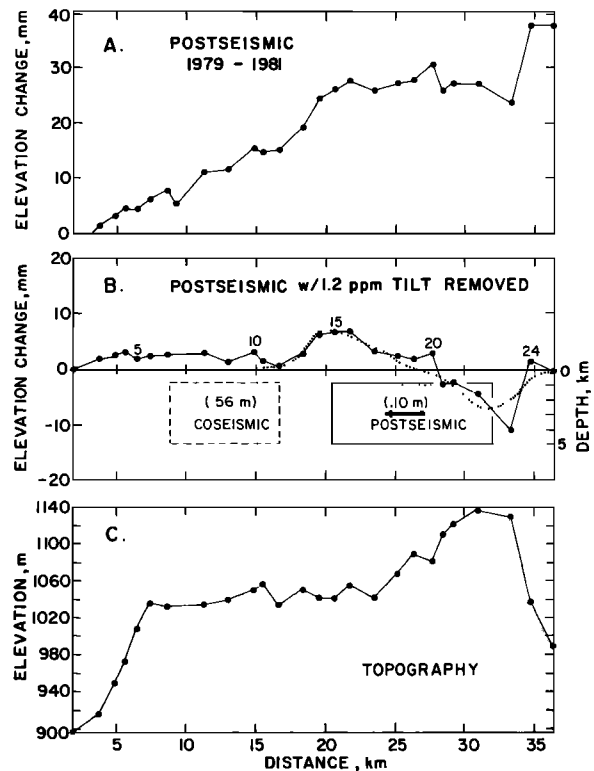

Fig. 12. Postseismic elevation changes along MAIN. (*a*) Observed changes. (*b*) Postseismic changes after fixing end-point elevations, with a postseismic fault model (dotted) to explain the leveling observations. (*c*) Route topography. Distance along leveling route is shown; this exaggerates the fault length.

changes and aftershocks over most of the region within about four fault lengths of the rupture zone requires that the preearthquake stress field was nearly uniform. The limited preseismic geodetic observations suggest that strain changes were not concentrated at the future epicentral area.

Ground rupture and creep. The coseismic surface offset represents less than 20% of the modeled buried fault slip; postseismic creep from the surface to depths of 1-2 km contributes an additional 10%. We infer from this result that surface offsets may provide poor guides to earthquake slip. The surface slip deficit is probably distributed at the surface over a wide zone. The location of ground breakage at Homestead Valley appears primarily limited to segments of fault zones where postearthquake stresses are favorably oriented; the surface faults do not necessarily merge into the seismic slip plane at depth.

Characteristics of the fault ends. We find that neither seismic nor aseismic slip greater than 20 mm took place beyond the ends of the seismic fault plane after the earthquakes sequence. The unslipped patches extend for one fault length (4-5 km) at both fault ends. However, aftershocks and possibly up to 100 mm of postseismic crustal creep occurred distal to the unslipped patches. We calculate that the unslipped regions were subject to static stress increases of at least 1.0-2.5 MPa. To sustain these stresses without producing aftershocks, the regions must have attained preearthquake stress levels 1.0-2.5 MPa lower than the surrounding region, or they must be stronger than the adjacent rocks.

APPENDIX: MODELING TRILATERATION OBSERVATIONS

We evaluate trilateration data by comparing observed line length changes dL_i to those of trial source models dL_i. The quality of fit is a function of the standard error associated with each observation, the consistency of all observations, and the redundancy of the network. Each line length change can be associated with a weight w_i, where $w_i = 1/2\sigma_i^2$. The standard deviation of an observation σ contains both random and systematic components of error and is defined by *Savage et al.* [1981]. The magnitude of the signal to be modeled (O) can be estimated by computing the mean amount by which the individual observations exceed their expected errors:

$$(O)^2 = [\sum_{i=1}^{n} (dL_i)^2 w_i] / n \qquad (A1)$$

where n is the number of line length changes; (O) is independent of both net geometry and fault models.

We compute (O-C) to calculate the internal consistency of the observations relative to assigned random errors. A least squares adjustment of the line length changes finds station displacements δL most compatible with all observations.

$$(O-C)^2 = [\sum_{i=1}^{n} (dL_i - \delta L_i)^2 w_i] / (n-2m+3) \qquad (A2)$$

The numerator divides the squared residuals by the squared standard deviation of the observations; the numerator would equal n

if each residual were equal to its standard deviation. The denominator reflects the network redundancy; a more redundant geometry allows a more comprehensive test of consistency. The denominator is equal to the computation degrees of freedom, where n is the number of line length observations, m is the number of stations, and 3 is the rank defect. The factor 2 derives from the two horizontal components of motion allowed for each station. The defect arises because rotation and displacement of the entire network in the north or east direction remain unconstrained. The quality of the source model is evaluated by the observed-modeled residuals

$$(O-M)^2 = [\sum_{i=1}^{n} (dL_i - dL_i)^2 w_i] / n \qquad (A3)$$

A model fit must satisfy the inequality (O-C) < (O-M) < (O). This criteria can be formalized to discriminate among models. We define two ratios for network and model evaluation. The network rms signal strength is

$$(S) = (O)/(O-C) \qquad (A4)$$

For example, if (S) = 2, then the signal is equal to 2 times the uncertainties caused by observational errors and network limitations, or 2σ. This ratio is independent of source models. To test the significance of (S), we calculate its probability function, which has an $F[(2m-3), (n-2m+3)]$ distribution

$$(S_1) = \frac{[n(0)^2 - (n-2m+3)(O-C)^2] / (2m-3)}{(O-C)^2} \qquad (A5)$$

The signal explained or satisfied by a given trial source model can be defined by

$$(M) = [(O) - (O-M)] / [(O) - (O-C)] \qquad (A6)$$

$M = 1$ when the model residuals equal the residuals of the network adjustment. The probability distribution function for (M) is

$$(M_1) = \frac{[n(O-M)^2 - (n-2m+3)(O-C)^2] / (2m-3)}{(O-C)^2} \qquad (A7)$$

REFERENCES

Boore, D. M., and W. S. Dunbar, Effect of the free surface on calculated stress drops, *Bull. Seismol. Soc. Am.*, *67*, 1661-1664, 1977.

Brown, R. D., P. L. Ward, and G. Plafker, Geologic and seismologic aspects of the Managua, Nicaragua, earthquakes of December 23, 1972, *U.S. Geol. Surv. Prof. Pap.*, *838*, 34 pp., 1973.

Brunner, F. K., On the analysis of geodetic networks for the determination of the incremental strain tensor, *Surv. Rev.*, *25*, 56-67, 1979.

Byerlee, J., Friction of rocks, *Pure Appl. Geophys.*, *116*, 615-626, 1978.

Chinnery, M. A., The stress changes that accompany strike-slip faulting, *Bull. Seismol. Soc. Am.*, *57*, 921-932, 1963.

Das, S., and C. H. Scholz, Off-fault aftershock clusters caused by shear stress increase?, *Bull. Seismol. Soc. Am.*, *71*, 1669-1675, 1981.

Dibblee, T. W., Geologic map of the Emerson Lake quadrangle, San Bernardino, California, *U.S. Geol. Surv. Misc. Geol. Invest.*, *Map I-490*, 1967.

Federal Geodetic Control Committee, *Specifications to Support Classification, Standards of Accuracy, and General Specifications of Geodetic Control Surveys*, National Oceanic and Atmospheric Administration, Rockville, Md., 1980.

Frank, F. C., Deduction of earth strains from survey data, *Bull. Seismol. Soc. Am.*, *56*, 35-42, 1966.

Hamilton, R. M., Aftershocks of the Borrego Mountain earthquake from April 12 to June 12, 1968, in The Borrego Mountain earthquake of April 9, 1968, *U.S. Geol. Surv. Prof. Pap.*, *787*, 31-54, 1972.

Hanks, T. C., and H. Kanamori, A moment magnitude scale, *J. Geophys. Res.*, *84*, 2348-2350, 1979.

Hill, R. L., J. C. Pechmann, J. A. Treiman, J. R. McMillan, T. W. Given, and J. E. Ebel, Geologic study of the Homestead Valley earthquake swarm of March 15, 1979, *Calif. Geol.*, *33*, 60-67, 1980.

Hutton, L. K., C. E. Johnson, J. C. Pechmann, J. E. Ebel, T. W. Given, D. M. Cole, and P. T. German, Epicentral locations for the Homestead Valley earthquake sequences, March 15, 1979, *Calif. Geol.*, *33*, 110-164, 1980.

Jachens, R. C., W. Thatcher, C. W. Roberts, and R. S. Stein, Correlation of changes in gravity, elevation and strain in southern California, *Science*, *219*, 1215-1217, 1983.

Jennings, C. W., Fault map of California, *Calif. Geol. Data Map 1*, Calif. Div. Mines and Geol., San Francisco, 1975.

Kadinsky-Cade, K., and R. J. Willemann, Towards understanding aftershock patterns: The basic pattern for strike slip earthquakes (abstract), *Eos Trans. AGU*, *63*, *384*, *1982*.

Kanamori, H., and D. L. Anderson, Theoretical basis of some empirical relations in seismology, *Bull. Seismol. Soc. Am.*, *65*, 1073-1095, 1975.

Lisowski, M. and W. H. Prescott, Short range distance measurements along the San Andreas fault system in central California, 1975 to 1977, *Bull. Seismol. Soc. Am.*, *71*, 1607-1624, 1981.

Mansinha, L., and D. E. Smylie, The displacement fields on inclined faults, *Bull. Seismol. Soc. Am.*, *61*, 1433-1440, 1971.

Moths, B. L., and W. L. Ellsworth, The California earthquake of 1857 and the seismic cycle (abstract), *Eos Trans. AGU*, *61*, 1030, 1980.

Prescott, W. H., An extension of Frank's method for obtaining crustal shear strains from survey data, *Bull. Seismol. Soc. Am.*, *66*, 1847-1853, 1976.

Prescott, W. H., M. Lisowski, and J. C. Savage, Geodetic measurement of crustal deformation on the San Andreas, Hayward, and Calaveras faults near San Francisco, California, *J. Geophys. Res.*, *86*, 10853-10869, 1981.

Savage, J. C., and W. H. Prescott, Precision of geodolite distance measurements for determining fault movement, *J. Geophys. Res.*, *78*, 6001-6008, 1973.

Savage, J. C., W. H. Prescott, M. Lisowski, and N. E. King, Strain accumulation in southern California, 1973-1980, *J. Geophys. Res.*, *86*, 6991-7001, 1981.

Scholz, C. H., M. Wyss, and S. W. Smith, Seismic and aseismic slip on the San Andreas fault, *J. Geophys. Res.*, *74*, 2049-2069, 1969.

Stein, R. S., Discrimination of tectonic displacement from slope-dependent errors in geodetic leveling from southern California, 1953-1979, in *Earthquake Prediction, An International Review, Maurice Ewing Ser.*, vol. 4, edited by D. W. Simpson and P. G. Richards, pp. 441-456, AGU, Washington, D.C., 1981.

Thatcher, W., and T. Hanks, Source parameters of southern California earthquakes, *J. Geophys. Res.*, *78*, 8547-8576, 1973.